 doi:10.20944/preprints202107.0143.v1

Article

Analysis Study of Hybrid Magnetic Equivalent Circuit of IP-MSM

In-Su Song[1], Byoung-Wook Jo[2] and Ki-Chan Kim [3,*]

[1] Dept. of Electrical Engineering, Hanbat National University 1; o1dlstn@naver.com
[2] Div. of Eco-friendly Vehicle R&D, Korea Automotive Technology Institute 2; jbwjbwjbw@naver.com
* Correspondence: kckim@hanbat.ac.kr; Tel.: Tel.: +82-42-821-1608

Abstract: Recently, the demand for electric vehicle is increasing worldwide due to eco-friendly policies and stricter emission regulations. As a traction motor for electric vehicle, interior permanent magnet synchronous motors are mainly used. For the design of the interior permanent magnet synchronous motor, the magnetic equivalent circuit method, which is a method of lumped constant circuit, and the finite element method, which is a method of distributed constant circuit, mainly are used. Magnetic equivalent circuit method is useful for simple design through fast and intuitive parameters, but it cannot derive the distribution of magnetic field. The finite element method can derive an accurate magnetic field distribution, but it takes a long time to analyze and it is difficult to analyze intuitive design parameters. In this paper, magnetic equivalent circuit method and Carter coefficient are mixed for rotor structure design. This design method will be called the hybrid magnetic equivalent circuit method. Intuitive design parameters are derived through this hybrid magnetic equivalent circuit method. We will derive the Air gap flux density distribution according to rotor shape, no-load induced voltage, and cogging torque, and compare and verify it with the finite element method.

Keywords: finite element method; hybrid magnetic equivalent circuit; the air gap flux density distribution; rotor shape.

1. Introduction

Recently, the demand for electric vehicle(EV)s is increasing worldwide due to eco-friendly policies and stricter emission regulations. As a traction motor for EVs, Interior Permanent Magnet Synchronous Motor(IPMSM) is mainly used [1-4].

The field of IPMSM does not require an excitation current because a permanent magnet is used. So the rotor loss is lower than that of other motors and high-efficiency operation is possible. In addition, the output density is higher than that of other motors because magnetic torque using the arranging force of the field and armature and reluctance torque using the salient polarity of the rotor occur at the same time. Finally, a wide range of operation range is possible by using the field-weakening operation characteristics. Because of these characteristics, it has multiple ratings and is suitable as a traction motor for an EV, where it is important to ensure the distance for one charge. At the same speed, high torque in the motor indicates high output, so it is a parameter that secures the distance for one charge and torque ripple is a source of electrical noise and vibration. Therefore, it is a factor that affects the driver's riding comfort [5-8].

The IPMSM for EVs has two operation areas. One is a constant torque range, and the other is a constant output operation range. The change in this range is very diverse depending on the motor design method [9-11]. For the design method of the IPMSM, the magnetic equivalent circuit method, which is a lumped constant circuit method, and the finite element method(FEM), which is a distributed circuit constant method are mainly used. In the magnetic equivalent circuit, the maximum speed, demagnetization details,

Preprints (www.preprints.org) | NOT PEER-REVIEWED | Posted: 6 July 2021 doi:10.20944/preprints202107.0143.v1

and maximum torque are simply determined by obtaining flux per pole, d-axis inductance, and q-axis inductance. After the simple design, the final design is made in consideration of the torque ripple, cogging torque, and voltage containing harmonic components in consideration of spatial and temporal magnetic field changed through FEM, spatial harmonic method, and etc. The magnetic equivalent circuit method is useful for simple design through fast and intuitive parameters, but cannot derive the magnetic field distribution. The FEM can derive an accurate magnetic field distribution, but it takes a long time to analyze and it is difficult to analyze intuitive design parameters. The FEM is used in order to verify the theory and the expertise of the designer is required in order to properly utilize the FEM. In other words, the advantages and limitations of existing design techniques are clear [12-16].

In this paper, magnetic equivalent circuit method and Carter coefficient are mixed for rotor structure design. This design method will be called the Hybrid Magnetic Equivalent Circuit(HMEC). Intuitive design parameters are derived through this HMEC. We will derive the air gap flux density distribution according to rotor shape, no-load induced voltage, and cogging torque, and compare and verify it with the FEM.

2. Calculation of the Air Gap Flux Density Distribution using Magnetic Equivalent Circuit and Carter Coefficient

2.1. Calculation of the Slotless Air Gap Flux Density Distribution by Permanent Magnet

Figure 1 shows three regions of the slotless flux line distribution by permanent magnet. θ_p, θ_a, and θ_b represent respectively the angle of pole arc, the angle between the starting point of the bridge from the center of the q-axis, and the angle between the bridge start point and end point. The slotless flux line distribution by the permanent magnet has a constant value at region of the pole arc, and the magnetic field is close to zero in region of the q-axis magnetic path and falls constantly region of a bridge as shown in Figure 1. Therefore, if it is treated as a line function that falls constantly region of barrier, function of the air flux density by permanent magnet as in Equation (1) and Figure 2(the slotless air gap flux density distribution) is derived. If Fourier series is applied to the function of Equation (1), Equation (2) and (3) are derived. The average air gap flux density is derived through the magnetic equivalent circuit.

$$B_g(\theta) = \begin{cases} 0 & 0 \le \theta < \theta_a \\ \dfrac{B_g}{\theta_b - \theta_a}(\theta - \theta_a) & \theta_a \le \theta < \theta_b \\ B_g & \theta_b \le \theta < \dfrac{\pi}{N_p} - \theta_b \\ -\dfrac{B_g}{\theta_b - \theta_a}\left(\theta - \left(\dfrac{\pi}{N_p} - \theta_a\right)\right) & \dfrac{\pi}{N_p} - \theta_b \le \theta < \dfrac{\pi}{N_p} - \theta_a \\ 0 & \dfrac{\pi}{N_p} - \theta_a \le \theta < \dfrac{\pi}{N_p} \end{cases} \quad (1)$$

$$B_{gn} = \frac{4B_g}{\pi N_p(\theta_b - \theta_a)(2n-1)^2}\left(\sin N_p\theta_b(2n-1) - \sin N_p\theta_a(2n-1)\right) \quad (2)$$

$$B_{gn}(\theta, \alpha) = \sum_{n=1}^{\infty} B_{gn} \sin N_p(\theta - \alpha)(2n-1) \quad (3)$$

Preprints (www.preprints.org) | NOT PEER-REVIEWED | Posted: 6 July 2021 doi:10.20944/preprints202107.0143.v1

Where B_g, n, α, B_{gn}, and N_p are respectively the average flux density of the air gap, harmonic order, angle of rotor position, Fourier coefficient of flux density and number of pole.

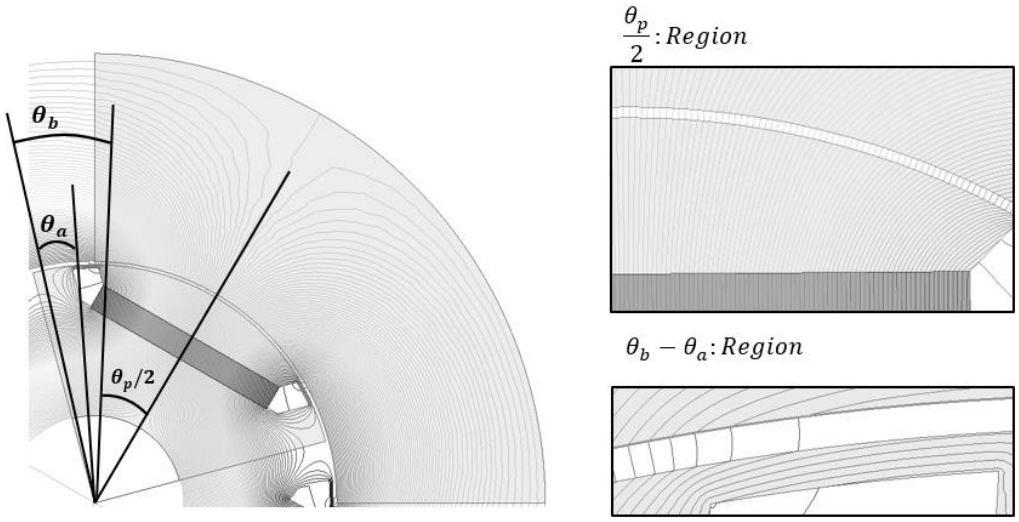

Figure 1. Three regions of the slotless flux line distribution by permanent magnet.

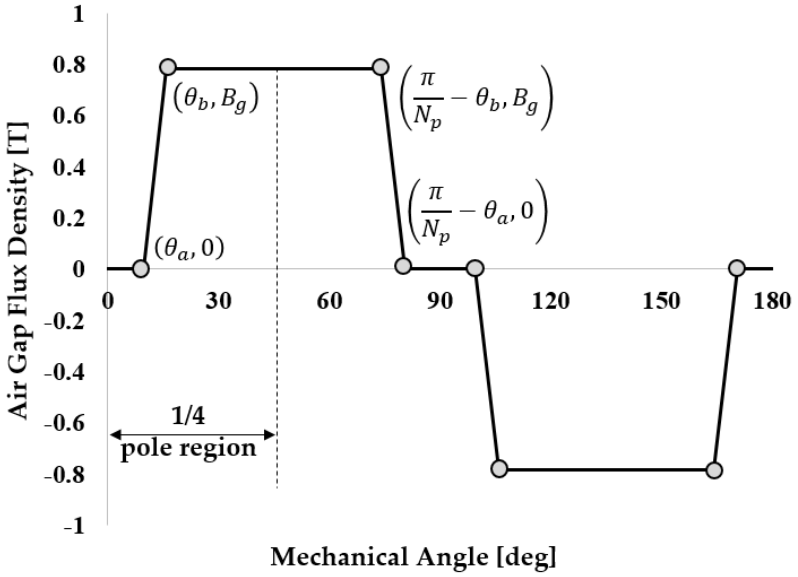

Figure 2. The slotless air gap flux density distribution.

Figure 3 shows the magnetic circuit of a slotless permanent magnet. The reluctance of the rotor core is very small compared to that of the air gap, barrier, and permanent magnet, so it is neglected. Since the reluctance of the stator core is connected in series with reluctance of the air gap as shown in Equation (4), it is treated as K_r. As shown in Equation (5), the barrier leakage of the permanent magnet is treated as K_l. Applying the flux distributive law, flux equation of the air gap is derived as in Equation (6). If Equation (6) is divided by area of the air gap, the average of the air gap flux density of Equation (7) is derived.

$$K_r = \frac{2R_g + R_{sy}}{2R_g} \tag{4}$$

Preprints (www.preprints.org) | NOT PEER-REVIEWED | Posted: 6 July 2021 doi:10.20944/preprints202107.0143.v1

$$K_l = \frac{2R_m \parallel R_{bl}}{2R_m} \tag{5}$$

$$\phi_g = \frac{\dfrac{1}{2K_r R_g}}{\dfrac{1}{2K_r R_g} + \dfrac{1}{R_b} + \dfrac{1}{2K_l R_m}} \phi_r \tag{6}$$

$$\frac{\phi_g}{A_g} = B_g \tag{7}$$

Where R_m, R_{bl}, R_b, R_g, R_{sy}, ϕ_g, and ϕ_r are respectively reluctance of permanent magnet, reluctance of a barrier, reluctance of a bridge, reluctance of the air gap, reluctance of stator yoke, flux of the air gap and residual flux.

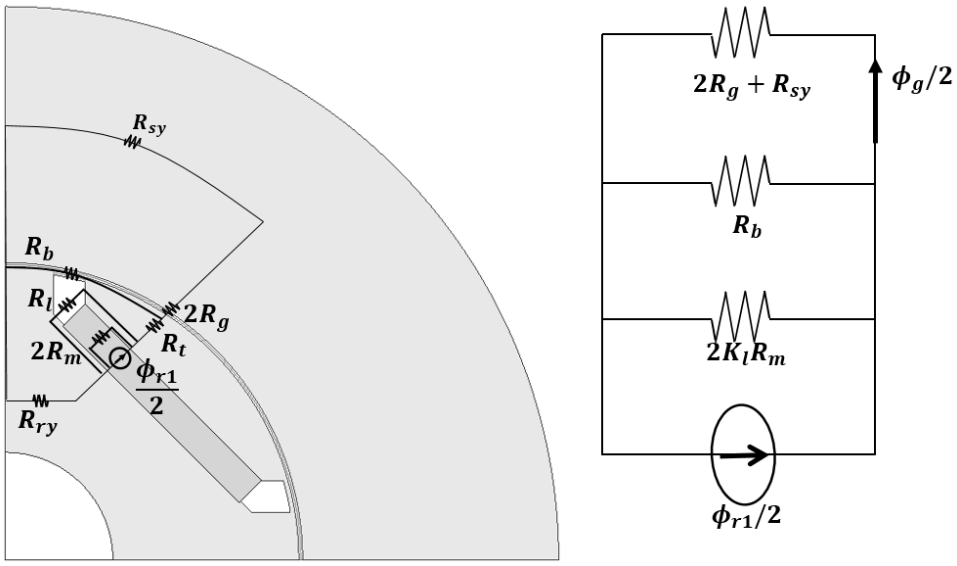

Figure 3. The magnetic circuit of a slotless permanent magnet.

2.2 Calculation of the Air Gap Flux Density Distribution by Permanent Magnet with Slot

The structure of a motor with slots as shown in Figure 4 is common. Figure 4 shows the flux line distribution by permanent magnets with slots. As can be seen from the Figure 4, when there is a slot, flux can be divided into two regions. One is the flux region that goes directly from the pole to the teeth, and the other is the flux region that goes from the pole to the teeth through the slot opening. The magnetic field is constant in the teeth region, but as can be seen from the flux in the slot open region, the length of the air gap increases toward the center of the slot opening and becomes the maximum length at the center. The distribution of the slot open region will be derived by applying the air gap length function of Carter's coefficient. In addition, the total average air gap flux density as such Equation (8) are derived through magnetic equivalent circuit as show in Figure 5

$$R_{sy} = R_{rt} = R_{ry} = 0 \tag{4}$$

$$R_k = K_{rk} R_{gk} \tag{5}$$

Preprints (www.preprints.org) | NOT PEER-REVIEWED | Posted: 6 July 2021 doi:10.20944/preprints202107.0143.v1

$$\phi_{gtotal}=\phi_{g1}+\phi_{g2}+\phi_{g3}+\phi_{g4} \tag{6}$$

$$B_{gk}=\frac{P_{gk}}{P_{total}}\frac{A_m}{A_{gk}}B_r \tag{7}$$

$$B_{gtotal}=\frac{\phi_{gtotal}}{A_{gtotal}} \tag{8}$$

Where R_{rt}, R_{ry}, P_{gk}, P_{total}, A_m, A_{gk}, A_{gtotal}, ϕ_{gtotal}, and B_{gtotal} are respectively reluctance of rotor teeth, reluctance of rotor yoke, permeance of the air gap corresponding to slot k, total permeance, area of permanent magnet, area of air gap corresponding to slot k, area of total air gap, total flux of air gap, and the total average air gap flux density.

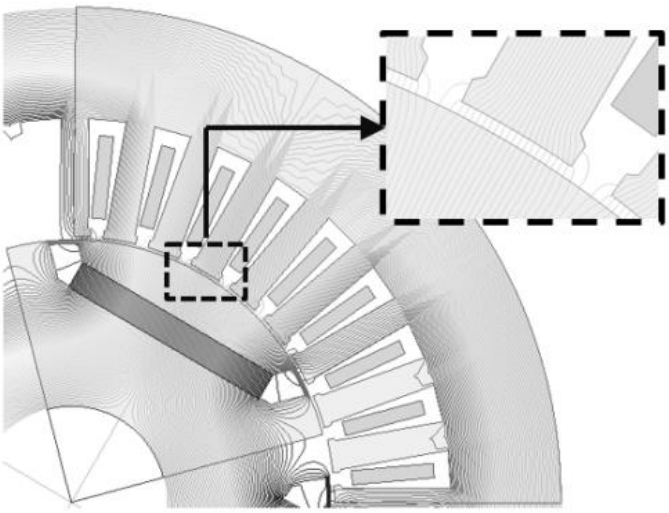

Figure 4. The flux line distribution by permanent magnets with slots.

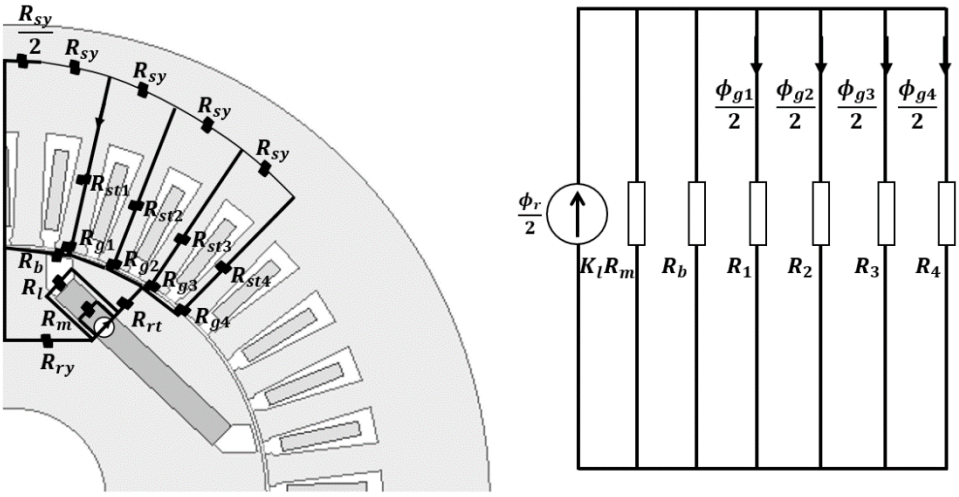

Figure 5. Magnetic equivalent circuit of permanent maget with slots.

Figure 6 shows the air gap flux line distribution per slot when there are slots. The average air gap flux density derived equation (12) is the total average of both the slot open and the teeth region. A transformation of the equation is necessary to obtain an accurate distribution. First, the air gap flux density in the teeth region like equation (14) can be obtained by multiplying equation (12) and (13) which is the flux distributive law of the

Preprints (www.preprints.org) | NOT PEER-REVIEWED | Posted: 6 July 2021 doi:10.20944/preprints202107.0143.v1

reluctance difference of teeth and the slot open region. Finally, the total air gap flux density in the teeth region as such equation (15) is derived.

$$C_{tk} = \frac{P_{gtk}}{P_{gtk} + 2P_{gso}} \frac{A_{gk}}{A_{gtk}} \tag{13}$$

$$B_{gtk} = C_{tk} B_{gk} \tag{14}$$

$$B_{gttotal} = \frac{\phi_{gttotal}}{A_{gttoal}} \tag{15}$$

Where C_{tk}, P_{gtk}, $2P_{gso}$, A_{gtk}, $A_{gttotal}$, $\phi_{gttotal}$, and $B_{gttotal}$ are correction factor of teeth about flux density of air gap, permeance of air gap corresponding to stator teeth of slot k, permeance of air gap corresponding to slot open of slot k, area of stator teeth, total area of stator teeth, total flux of stator teeth, and total flux density of stator teeth.

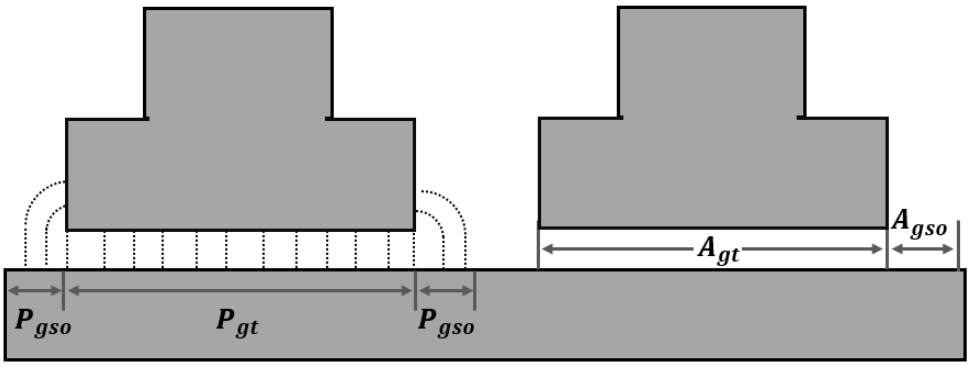

Figure 6. the air gap flux line distribution per slot when there are slots.

The function of the air gap length of the slot open region is expressed as equation (16). In order to derive function of the slot fator, the magnetic circuit equation obtained by functionalizing the air gap length is divided into the magnetic circuit equation before functionalization. If these equations are arranged, the function equation of the slot factor like equation (17) is derived. However, this slot factor function does not reflect the saturation of flux density of the shoe part as shown in Figure 6(a). Therefore, by applying the slot open range of Hanselman, the slot open is changed to 0.7, which is larger than the actual 0.5, and changed to Equation (18) [14]. The final slot factor function like equation (19) and (20) is derived. Applying this expression to the Fourier series gives Equation (21), (22), (23). Figure 6(b) shows the slot factor derived through the HMEC and FEM.

$$\frac{g(\theta)}{g} = \begin{cases} 1 & |\theta| \le \frac{\theta_t}{2} \\ 1 + \frac{\pi}{2}\frac{r_{si}}{g}\left(|\theta| - \theta_t\right) & \frac{\theta_t}{2} \le |\theta| < \frac{\theta_{sp}}{2} \end{cases} \tag{16}$$

$$G_{sl}(\theta) = \frac{B_{gt}(\theta)}{B_{gt}} = \frac{\frac{1}{g} + \frac{2C_t K_r}{\mu_0 A_g}\left(\frac{1}{R_b} + \frac{1}{2K_l R_m}\right)}{\frac{1}{g} + \frac{2C_t K_r}{\mu_0 A_g}\left(\frac{1}{R_b} + \frac{1}{2K_l R_m}\right)\frac{g(\theta)}{g}} \tag{17}$$

Preprints (www.preprints.org) | NOT PEER-REVIEWED | Posted: 6 July 2021 doi:10.20944/preprints202107.0143.v1

$$\frac{\theta_{tr}}{2} = \frac{\theta_{sp}}{2} - 0.7\theta_{so} \tag{18}$$

$$G_{\min} = \frac{\frac{1}{g} + \frac{2C_t K_r}{\mu_0 A_g}\left(\frac{1}{R_b} + \frac{1}{2K_l R_m}\right)}{\frac{1}{g} + \frac{2C_t K_r}{\mu_0 A_g}\left(\frac{1}{R_b} + \frac{1}{2K_l R_m}\right)\left(1 + \frac{\pi r_{si}\theta_{so}}{4g}\right)} \tag{19}$$

$$G_{sl}(\theta) = \begin{cases} 1 & |\theta| \le \frac{\theta_{tr}}{2} \\ \frac{1+G_{\min}}{2} + \frac{1-G_{\min}}{2}\cos\left(\frac{\pi\left(|\theta| - 0.5\theta_{tr}\right)}{0.7\theta_{so}}\right) & \frac{\theta_t}{2} \le |\theta| < \frac{\theta_{sp}}{2} \end{cases} \tag{20}$$

$$G_{slo} = \frac{N_s}{\pi}\left(\frac{\theta_{tr}}{2} + \frac{0.7\theta_{so}}{2}\right)\left(1 + G_{\min}\right) \tag{21}$$

$$G_{s\ln} = \left(1 + \frac{N_s}{nN_s + \frac{\pi}{0.7\theta_{so}}} + \frac{N_s}{nN_s - \frac{\pi}{0.7\theta_{so}}}\right)\frac{(1-G_{\min})}{2\pi}\sin(N_s\frac{\theta_{tr}}{2}n) \tag{22}$$

$$G_{s\ln}(\theta) = G_{slo} + \sum_{n=1}^{\infty} G_{s\ln}\cos N_s n\theta \tag{23}$$

Where $G_{s\ln}(\theta)$, θ_t, θ_{sp}, θ_{so}, θ_{tr}, r_{si}, $G_{\min}$, and N_s are function of slot factor, stator teeth pitch, slot pitch, slot open pitch, stator teeth pitch considering saturation of shoe, inner radius of stator, minimum value of slot factor, and the number of slots

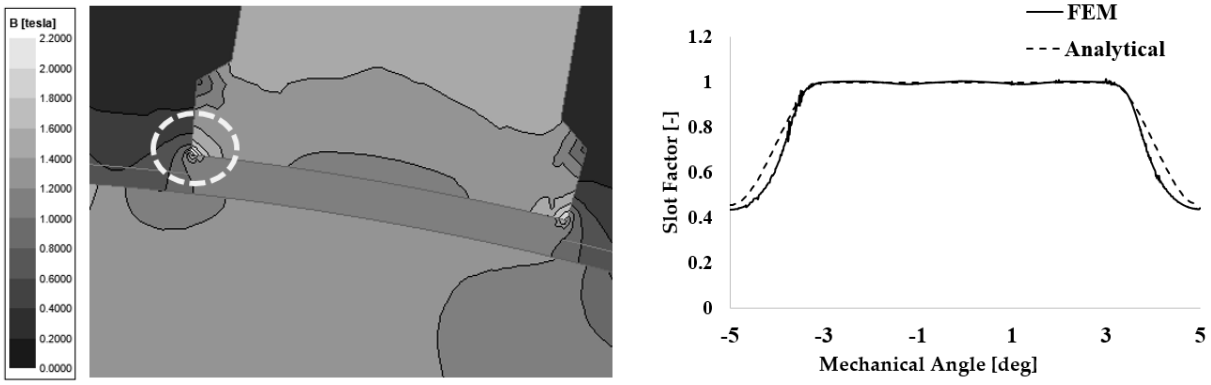

(**a**) (**b**)

Figure 7. the magnetic field distribution: (a)flux density of the teeth and shoe; (b)slot factor.

Figure 8 shows comparison of the air gap flux density distribution by permanent magnet with slots derived from HMEC and FEM. It can be seen that the HMEC and FEM have similar waveforms. No-load induced voltage, flux linkage, and cogging torque can be derived through Equation (24).

$$B_{gn}^{'}(\theta,\alpha) = B_{gtn}(\theta,\alpha)G_{s\ln}(\theta) \tag{24}$$

Preprints (www.preprints.org) | NOT PEER-REVIEWED | Posted: 6 July 2021 doi:10.20944/preprints202107.0143.v1

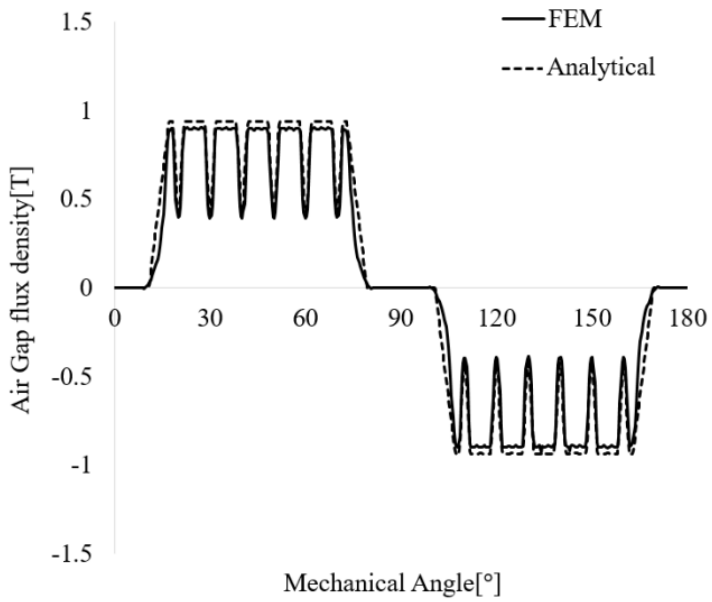

Figure 8. comparison of the air gap flux density distribution by permanent magnet with slots derived from HMEC and FEM**.**

2.3 Calculation of Flux Linkage, No-load Induced Voltage , and Cogging Torque

Figure 9 shows the flux linkage derived through HEMC and the FEM. Equation (25) represents the flux linkage of one coil. In the case of this model, the number of slots per phase per pole is three. Therefore, the flux linkage in one phase can be obtained as in Equation (26). By differentiating Equation (26), the no-load induced voltage can be derived as such Equation (27). Figure 10 shows comparison of the no-load induced voltage derived from HMEC and FEM**.** The cogging torque as such equation (29) is derived by differentiating the air gap energy of equation (28). Fig. 11 shows comparison of the cogging torque waveform derived from HMEC and FEM.

$$\lambda_{coil}(\alpha) = N_{coil} r_{si} L_{stk} \int_0^{\frac{\pi}{N_p}} B_{gtn}(\theta,\alpha) G_{s\ln}(\theta) d\theta \tag{25}$$

$$\lambda_{ph}(\theta,\alpha) = \lambda_{coil1}(\theta-\theta_{sp},\alpha) + \lambda_{coil2}(\theta,\alpha) + \lambda_{coil3}(\theta+\theta_{sp},\alpha) \tag{26}$$

$$E_{ph} = -\frac{d\lambda_{ph}(\alpha)}{d\alpha} \tag{27}$$

$$W(\alpha)_g = \int_0^{L_{stk}} \int_{r_{ro}}^{r_{si}} \int_0^{2\pi} B_{gn}^{'2}(\theta,\alpha) G_{s\ln}^2(\theta) d\theta \tag{28}$$

$$T_{cog}(\alpha) = \frac{dW(\alpha)}{d\alpha} = \frac{d}{d\alpha}\left(\frac{L_{stk}}{4\mu_0}\right)\left(r_{si}^2 - r_{ro}^2\right)\int_0^{2\pi} B_{gn}^{'2}(\theta,\alpha) G_{s\ln}^2(\theta) d\theta \tag{29}$$

Where N_{coil}, L_{stk}, λ_{coil} , and λ_{ph} are turns of one coil, stack length, flux linkage of one coil, and flux linkage of one phase.

Preprints (www.preprints.org) | NOT PEER-REVIEWED | Posted: 6 July 2021 doi:10.20944/preprints202107.0143.v1

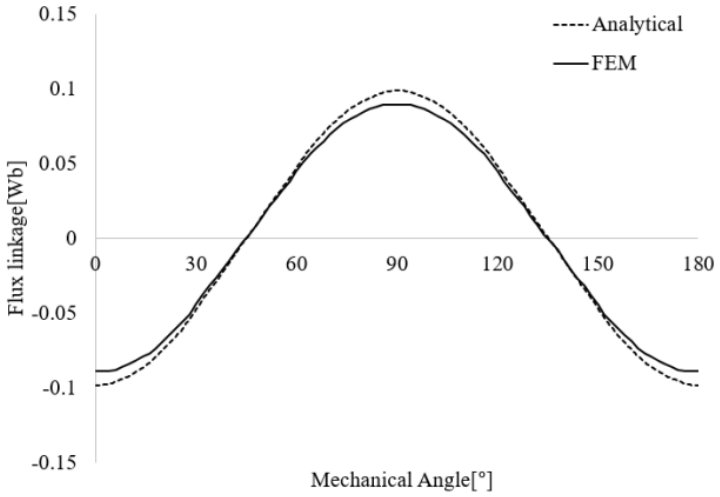

Figure 9. comparison of the flux linkage derived from HMEC and FEM.

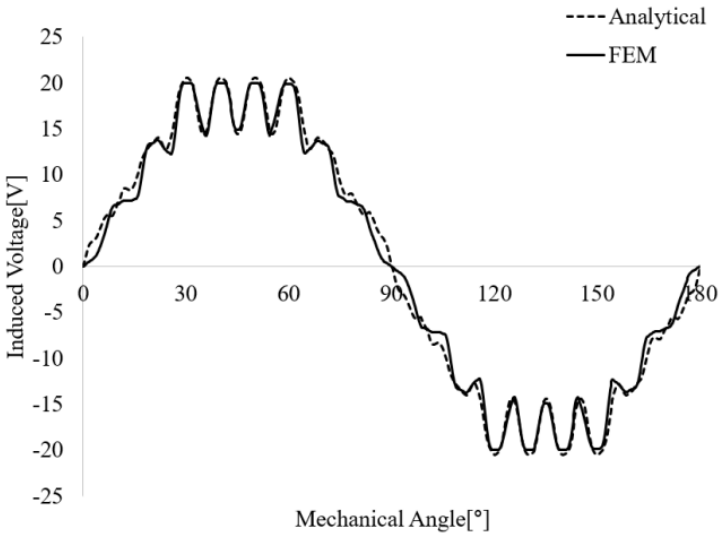

Figure 10. comparison of the no-load induced voltage derived from HMEC and FEM.

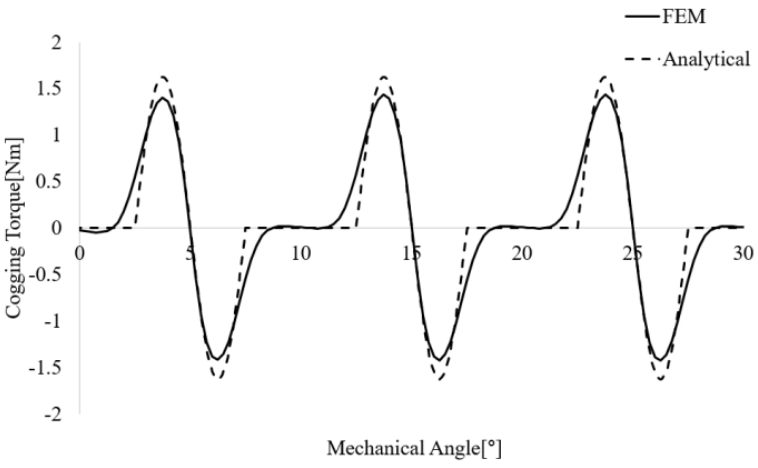

Figure 11. comparison of the cogging torque derived from HMEC and FEM.

3. Calculation of the Air Gap Flux Density Distribution by Permanent Magnet according to Rotor Type

3.1 Calculation of the Air Gap Flux Density Distribution by Permanent Magnet V-type Rotor

Preprints (www.preprints.org) | NOT PEER-REVIEWED | Posted: 6 July 2021 doi:10.20944/preprints202107.0143.v1

Figure 12 shows magnetic equivalent circuit of V-type rotor. As shown in Figure 12, unlike the bar shape, the V shape has an inner bridge and barrier part on the central axis of the pole arc. In addition, by adjusting the angle of the magnet, the area of the permanent magnet can be increased compared to the bar shape. Figure 13 shows comparison of flux density distribution of the air gap with bar-type and V-type rotor with slots. Since area of the air gap and the permanent magnet is the same, as shown in the Figure 13, the difference of the two rotors is the difference of the leakage flux according to the presence or absence of the inner bridge and barrier. Therefore, if the area of the permanent magnet is not increased in the V shape, the flux per pole drops as shown in Equation (30) and (31) due to the inner leakage flux. Also, as shown in Equation (32), as the leakage of the bridge and barrier change, the value decreases and the cogging torque changes as shown in Figure 14. Figure 14 shows comparison of cogging torque with bar-type and V-type rotor with slots.

$$K_{ltotal} = \frac{2R_m \parallel R_{il} \parallel R_{ol}}{2R_m} \tag{30}$$

$$\phi_g = \frac{\frac{1}{2K_r R_g}}{\frac{1}{2K_r R_g} + \frac{1}{2R_{ib}} + \frac{1}{R_{ob}} + \frac{1}{2K_{ltotal} R_m}} \phi_r \tag{31}$$

$$G_{\min} = \frac{\frac{1}{g} + \frac{2C_t K_r}{\mu_0 A_g}\left(\frac{1}{2R_{ib}} + \frac{1}{R_{ob}} + \frac{1}{2K_{ltotal} R_m}\right)}{\frac{1}{g} + \frac{2C_t K_r}{\mu_0 A_g}\left(\frac{1}{2R_{ib}} + \frac{1}{R_{ob}} + \frac{1}{2K_{ltotal} R_m}\right)\left(1 + \frac{\pi r_{si}\theta_{so}}{4g}\right)} \tag{32}$$

Where R_{il}, R_{ol}, R_{ib}, and R_{ob}, are reluctance of inner and outer barrier, and inner and outer bridge.

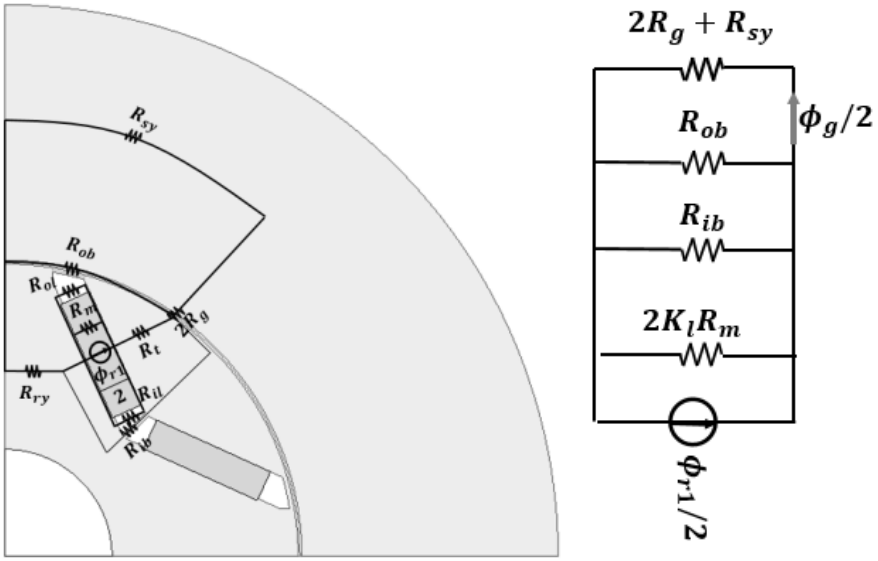

Figure 12. magnetic equivalent circuit of V-type rotor.

Table 1. Comparison of magnetic field distribution parameters of bar-type and V-type rotor when there is a slot.

Type	Bar	V	Unit

Preprints (www.preprints.org) | NOT PEER-REVIEWED | Posted: 6 July 2021 doi:10.20944/preprints202107.0143.v1

K_{ltotal}	0.9898	0.9891	[-]
R_{btotal}	1,051,237	831,420	[AT/Wb]
$B_{gttotal}$	922	904.22	[mT]
G_{min}	0.447	0.438	[-]

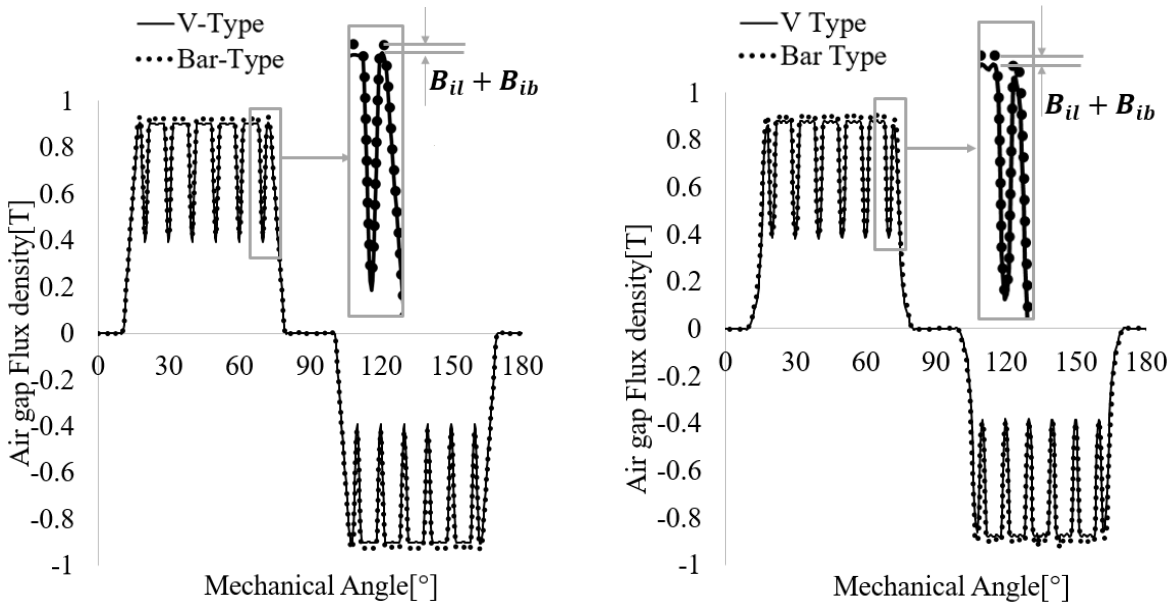

(**a**) (**b**)

Figure 13. comparison of flux density distribution of the air gap with bar-type and V-type rotor with slots: (a) HMEC; (b)FEM.

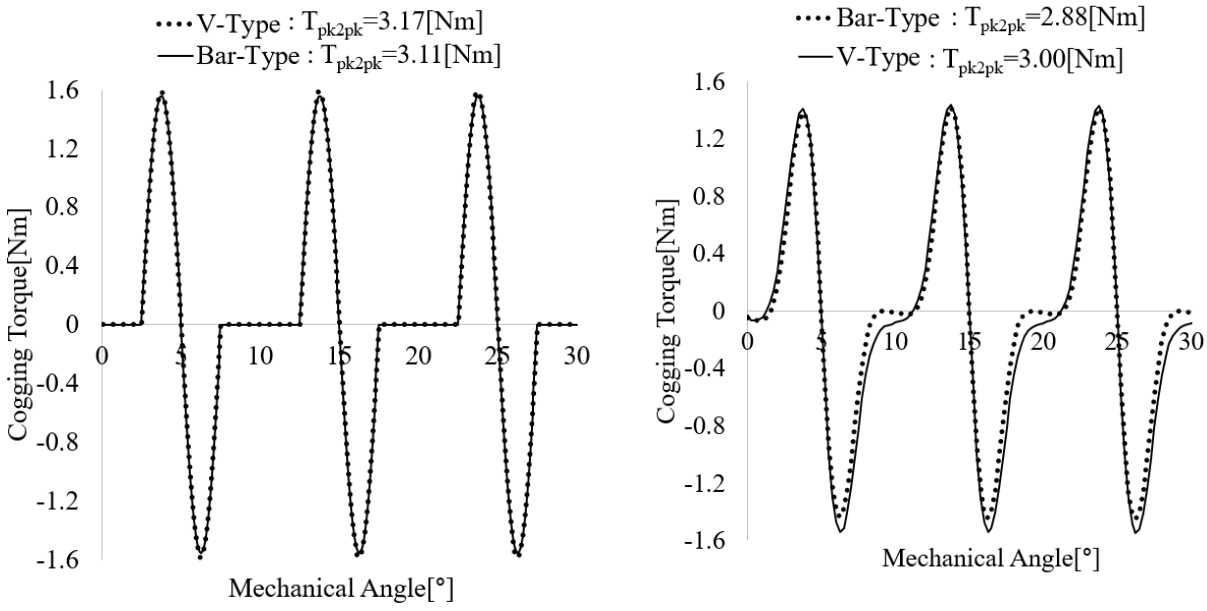

(**a**) (**b**)

Figure 14. comparison of cogging torque with bar-type and V-type rotor with slots: (a) HMEC; (b)FEM.

3.2 Calculation of Flux Density Distribution of the Air Gap by Permanent Magnet Double-layer type rotor

Preprints (www.preprints.org) | NOT PEER-REVIEWED | Posted: 6 July 2021 doi:10.20944/preprints202107.0143.v1

Figure 15 shows the air gap flux density distribution of slotless double-layer bar-type rotor. In the double-layer bar-type rotor, as shown in the figure 15, the air gap region corresponding to the permanent magnet should be divided into two parts.

$$B_g(\theta)=\begin{cases} 0 & 0\le\theta<\theta_a \\ \dfrac{B_{g1}}{(\theta_b-\theta_a)}(\theta-\theta_a) & \theta_a\le\theta<\theta_b \\ B_{g1} & \theta_b\le\theta<\theta_c \\ \dfrac{B_{g1}}{(\theta_d-\theta_c)}(\theta-\theta_c) & \theta_c\le\theta<\theta_d \\ B_{g2} & \theta_d\le\theta<\dfrac{\pi}{N_p}-\theta_d \\ -\dfrac{B_{g2}}{(\theta_d-\theta_c)}\left(\theta-\left(\dfrac{\pi}{N_p}-\theta_c\right)\right) & \dfrac{\pi}{N_p}-\theta_d\le\theta<\dfrac{\pi}{N_p}-\theta_c \\ B_{g1} & \dfrac{\pi}{N_p}-\theta_c\le\theta<\dfrac{\pi}{N_p}-\theta_b \\ -\dfrac{B_{g1}}{(\theta_b-\theta_a)}\left(\theta-\left(\dfrac{\pi}{N_p}-\theta a\right)\right) & \dfrac{\pi}{N_p}-\theta_b\le\theta<\dfrac{\pi}{N_p}-\theta_a \\ 0 & \dfrac{\pi}{N_p}-\theta_a\le\theta<\dfrac{\pi}{N_p} \end{cases} \tag{33}$$

$$\begin{aligned} B_{gn}=&\frac{4B_{g1}}{\pi N_p(\theta_b-\theta_a)(2n-1)^2}\left(\sin N_p\theta_b(2n-1)-\sin N_p\theta_a(2n-1)\right) \\ &+\frac{4\left(B_{g2}-B_{g1}\right)}{\pi N_p(\theta_d-\theta_c)(2n-1)^2}\left(\sin N_p\theta_d(2n-1)-\sin N_p\theta_c(2n-1)\right) \end{aligned} \tag{34}$$

Equation (33) shows the magnetic flux density distribution by permanent magnet. Applying this expression to the Fourier series gives Equation (34) and (35). Although the flux per pole drops when the same permanent magnet is used, the harmonic order is reduced because the air gap flux density can be made closer to sinusoidal. The double-layer type rotor can be classified into three types. As shown in Figure 15, one is a Double-layer Bar(DB) structure, the other is a Double-layer V(DV) structure, and the last is a delta structure mixed bar & V-type structure. The amount of permanent magnet used, area of the air gap, and area of the permanent magnet are the same. Therefore, the amount of flux per pole in the two regions varies depending on the presence of the inner barrier and bridge. By applying these conditions, the flux density of the air gap for each two-layer shape in Table 2 was calculated.

Preprints (www.preprints.org) | NOT PEER-REVIEWED | Posted: 6 July 2021 doi:10.20944/preprints202107.0143.v1

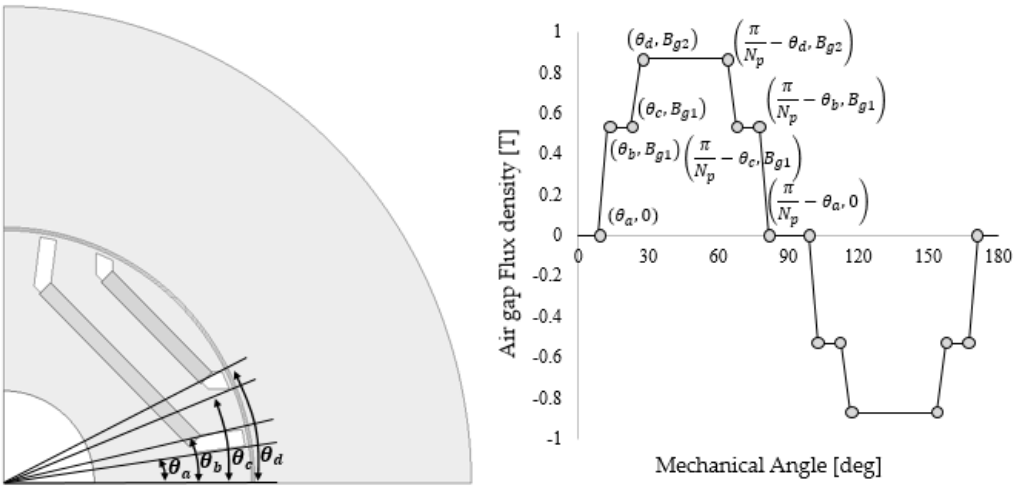

Figure 15. Air gap flux density distribution of slotless double-layer bar rotor.

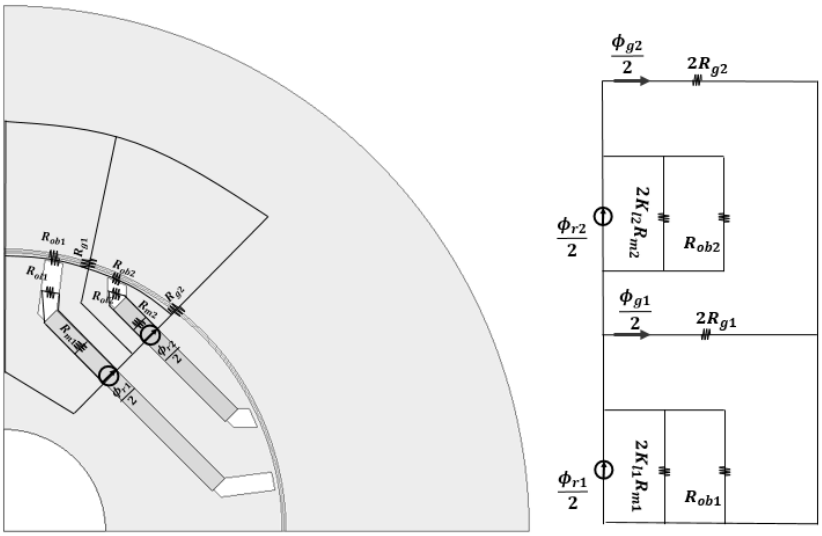

(a)

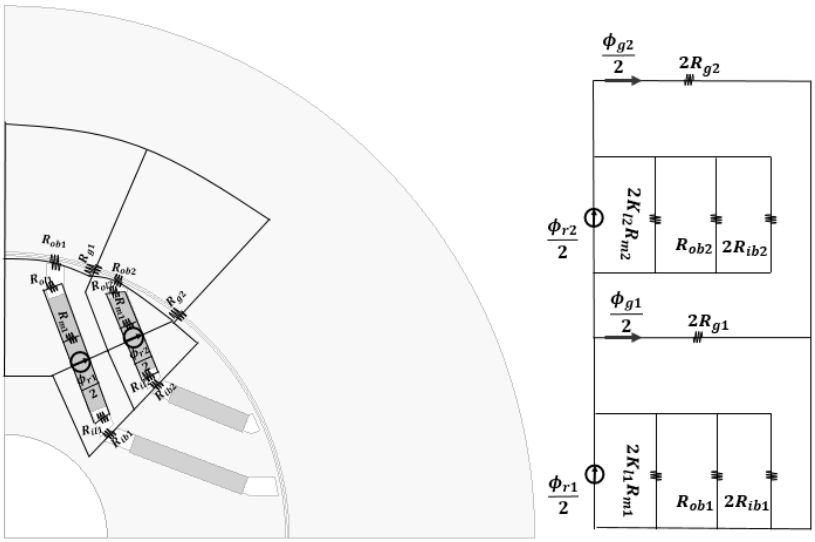

(b)

Preprints (www.preprints.org) | NOT PEER-REVIEWED | Posted: 6 July 2021 doi:10.20944/preprints202107.0143.v1

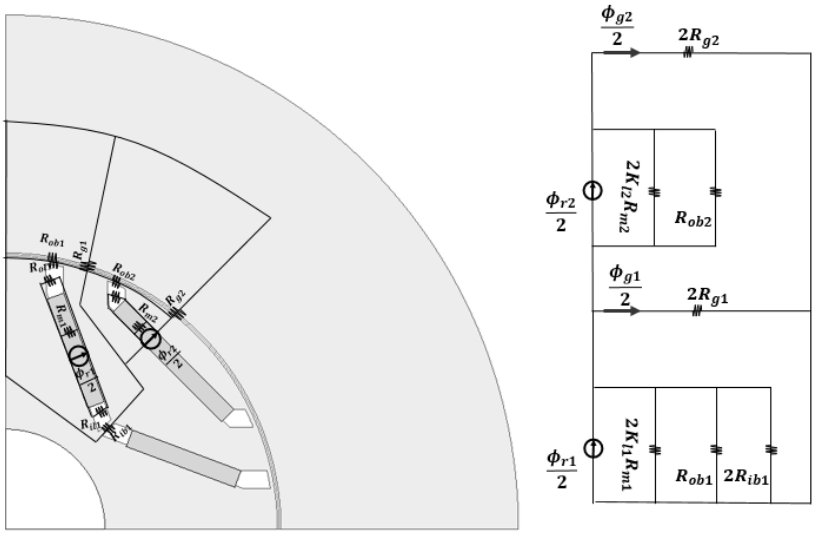

(c)

Figure 16. magnetic equivalent circuit of permanent magnet when there is no slot for each two-layer rotor: (a)DB; (b)DV; (c)Delta.

Figure 16 shows magnetic equivalent circuit of permanent magnet when there is no slot for each two-layer rotor. Table 2 shows equations of parameters of air gap flux density distribution according to double layer rotor. Because reluctance of the rotor and stator core were ignored and the effective area difference of the air gap of HMEC and FEM, the value calculated by the HMEC had an error from 2.54 [%] to 3.53 [%] than that of the FEM as show in Table 3 which is comparison of magnetic field distribution parameters of double layer rotor when there is a slot. In addition, Flux density of the air gap in the DB without the inner bridge and barrier was the highest and the DV had the smallest. The delta shape had a medium flux per pole, but there was no barrier or bridge in the two-layer part, so the magnetic flux was large in the inner and the outer magnetic flux was rather smaller than that of the double-layered V-shape.

Table 2. Equations of parameters of air gap flux density distribution according to double layer rotor.

	Equation
The air gap flux	$\frac{\Phi_{g1}}{2}=\frac{\Phi_{g11}}{2}-\frac{\Phi_{g12}}{2}$ $\frac{\Phi_{g2}}{2}=\frac{\Phi_{g12}}{2}+\frac{\Phi_{g22}}{2}$
The air gap flux density	$B_{g1}=\frac{\Phi_{g1}}{A_{g1}}$ $B_{g2}=\frac{\Phi_{g2}}{A_{g2}}$
Slot factor	$G(\theta)=\frac{B_{g1}(\theta)+B_{g2}(\theta)}{B_{g1}+B_{g2}}$
DB	

Preprints (www.preprints.org) | NOT PEER-REVIEWED | Posted: 6 July 2021 doi:10.20944/preprints202107.0143.v1

	$\frac{\Phi_{g11}}{2} = \frac{P_{g1}}{P'_{m1} + P_{ob1} + P_{g1} + P_A} \frac{\Phi_{r1}}{2}$ $\frac{\Phi_{g21}}{2} = \frac{P_A}{P'_{m1} + P_{ob1} + P_{g1} + P_A} \frac{\Phi_{r1}}{2}$ $\frac{\Phi_{g12}}{2} = \frac{P_{g1}}{P'_{m1} + P_{ob1} + P_{g1}} \frac{P_B}{P'_{m2} + P_{ob2} + P_B} \frac{\Phi_{r2}}{2}$ $\frac{\Phi_{g22}}{2} = \frac{P_B}{P'_{m2} + P_{ob2} + P_B} \frac{\Phi_{r2}}{2}$ $P_A = 2K_{l2}R_{m2} \| R_{ob2} + 2R_{g2}$ $P_B = 2K_{l1}R_{m1} \| R_{ob1} \| 2R_{g1} + 2R_{g2}$
DV	$\frac{\Phi_{g11}}{2} = \frac{P_{g1}}{P'_{m1} + P_{ob1} + P_{ib1} + P_{g1} + P_A} \frac{\Phi_{r1}}{2}$ $\frac{\Phi_{g21}}{2} = \frac{P_A}{P'_{m1} + P_{ob1} + P_{ib1} + P_{g1} + P_A} \frac{\Phi_{r1}}{2}$ $\frac{\Phi_{g12}}{2} = \frac{P_{g1}}{P'_{m1} + P_{ob1} + P_{ib1} + P_{g1}} \frac{P_B}{P'_{m2} + P_{ob2} + P_{ib2} + P_B} \frac{\Phi_{r2}}{2}$ $\frac{\Phi_{g22}}{2} = \frac{P_B}{P'_{m2} + P_{ob} + P_{ib} + P_B} \frac{\Phi_{r2}}{2}$ $P_A = 2K_{l2}R_{m2} \| R_{ob2} \| R_{ib2} + 2R_{g2}$ $P_B = 2K_{l1}R_{m1} \| R_{ob1} \| R_{ib1} \| 2R_{g1} + 2R_{g2}$
Delta	$\frac{\Phi_{g11}}{2} = \frac{P_{g1}}{P'_{m1} + P_{ob1} + P_{ib1} + P_{g1} + P_A} \frac{\Phi_{r1}}{2}$ $\frac{\Phi_{g21}}{2} = \frac{P_A}{P'_{m1} + P_{ob1} + P_{ib1} + P_{g1} + P_A} \frac{\Phi_{r1}}{2}$ $\frac{\Phi_{g12}}{2} = \frac{P_{g1}}{P'_{m1} + P_{ob1} + P_{ib1} + P_{g1}} \frac{P_B}{P'_{m2} + P_{ob} + P_D} \frac{\Phi_{r2}}{2}$ $\frac{\Phi_{g22}}{2} = \frac{P_B}{P'_{m2} + P_{ob} + P_B} \frac{\Phi_{r2}}{2}$ $P_A = 2K_{l2}R_{m2} \| R_{ob2} + 2R_{g2}$ $P_B = 2K_{l1}R_{m1} \| R_{ob1} \| 2R_{g1} + 2R_{g2}$

Preprints (www.preprints.org) | NOT PEER-REVIEWED | Posted: 6 July 2021 doi:10.20944/preprints202107.0143.v1

Table 3. Comparison of calculation of parameters of the air gap flux density distribution according to double layer rotor.

	HMEC			FEM			
Type	**DB**	**DV**	**Delta**	**DB**	**DV**	**Delta**	**Unit**
C_{t1}	1.16						[-]
C_{t2}	1.17						
G_{min}	0.454	0.445	0.443	0.436	0.436	0.437	
B_{gt1}	594	582	536	562	545	508	[mT]
B_{gt2}	987	918	975	960	890	947	

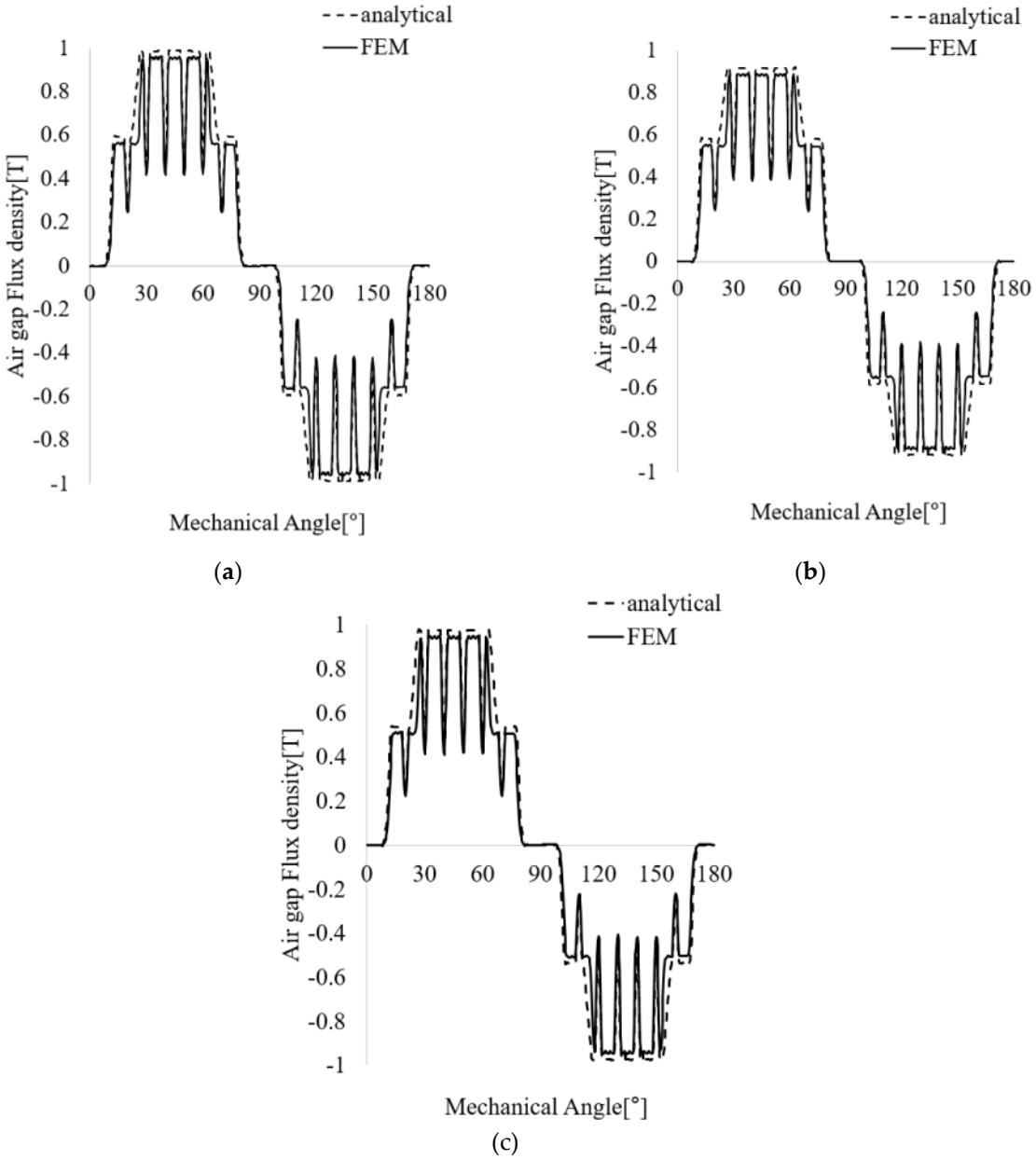

Figure 17. Comparison of flux density distribution when there is a slot for each two-layer shape derived through HMEC and FEM: (a)DB; (b)DV; (c)Delta.

4. Conclusion

In this paper, we propose a hybrid magnetic equivalent circuit method, that is, a design method that combines the spatial harmonic method and the magnetic circuit method.

The magnetic field distribution according to the rotor type was derived through the hybrid magnetic equivalent circuit method, and the cogging torque and no-load counter electromotive force were derived through the magnetic field distribution map. Through the hybrid magnetic equivalent circuit method, the existing design method was supplemented with reduced analysis time and intuitive design parameters. However, an error occurred due to the difference in effective air gap area due to ignoring the iron core resistance of the rotor and the stator and the effect of bridge magnetic saturation. Since this error is less than 5 [%] in error range compared to the finite element method, the hybrid magnetic equivalent circuit method is proposed.

Acknowledgments: This work was supported by the Technology Innovation Program (20011435, Development of large capacity Etransaxle and application technology of 240kW class in integrated rear axle for medium and large commercial vehicles) funded By the Ministry of Trade, Industry & Energy(MOTIE, Korea)

This work was supported by the Korea Institute of Energy Technology Evaluation and Planning(KETEP) and the Ministry of Trade, Industry & Energy(MOTIE) of the Republic of Korea (No. 20204030200080).

References

1. Liang Chen, David Hopkinson, Jiabin Wang, Andrew Cockburn, Martin Sparkes, and William O'Neill, "Reduced Dysprosium Permanent Magnets and Their Application in Electric Vehicle Traction Motors. IEEE Transactions on Magnetics, Vol. 51, No. 11, Art. No. 8109004, Nov. 2015.
2. Kim MJ, Cho SY, Lee KD, Lee JJ, Han JH, Jeong TC, and et al, "Torque Density Elevation in Concentrated Winding Interior PM Synchronous Motor With Minimized Magnet Volume", IEEE Transactions on Magnetics", Vol. 49, No. 47, pp. 3334-3337, Jul. 2013.
3. Ryokuke Akaki, Yasuhito Takahashi, Koji Fujiwara, Makoto Matsushita, Norio Takahashi, and Masatsugu Mortia, "Effect of Magnetic Property in Bridge Area IPM Motors on Torque Characteristics", IEEE Transactions on Magnetics, Vol. 49, No. 5, pp. 2335-2338, May. 2013.
4. Ho-Chang Jung, Gyeong-Jae Park, Deok-Jin Kim, and Sang-Yong Jung, "Optimal Design and Validation of IPMSM for Maximum Efficiency Distribution Compatible to Energy Consumption Areas of HD-EV", Vol. 53, No. 6, Art. No. 8201904, Jun. 2017.
5. Gyu-Hong Kang, Young-Dae Son, and Jin Hur, "A Novel Cogging Reduction Method for Interior-Type Permanent-Magnet Motor", IEEE Transactions on Industry Applications, Vol. 45, No. 1, pp. 161-167, Jan./Feb. 2009.
6. Jin Hur, Jin-Wook Reu, Byeong-Woo Kim, and Gyu-Hong Kang, "Vibration Reduction of IPM-Type BLDC Motor Using Negative Thrid Harmonic Elimination Method of Air-Gap Flux Density", IEEE Transactions on Industry Applications, Vol. 47, No. 3, pp. 1300-1309, May/June 2011.
7. Hsing-Cheng Yu, Bo-Syun Yu, Jen-te Yu, and Cheng Kai Lin, "A dual Notched Design of Radial-flux Permanent Magnet Motors with Low Cogging Torque and Rare Earth Material",. IEEE Transactions on Magnetics, Vol. 50, No. 11, Art. No. 8203104, Nov. 2014.
8. Sai Sudheer Reddy Bonthu, Md. Tawhid Bin Tarek, and Seugdeog Choi, "Optimal Torque Ripple Reduction Technique for Outer Rotor Permanent Magnet Synchronous Reluctance Motors", IEEE Transactions on Energy Conversion, Vol. 33, No. 3, pp. 1187-1192, Sep. 2018.
9. Jung-Min Mun, Gyeong-Jae Park, Sang-Hyeok Seo, Dae-Woo Kim, Yong-Jae Kim, and Sang-Yong Jung, "Design Characteristics of IPMSM With Wide Constant Power Speed Range For EV Traction", IEEE Transactions on Magnetics, Vol. 53, No. 6, Art. No. 8105104, Jun. 2017.
10. Won-Ho Kim, Kwang-Soo Kim, Seung-Joo Kim, Dong-Woo Kang, Sung-Chul Go, Yon-Do Chun, and J. Lee, "Optimal PM Design of PMA-SynRM for Wide Constant-Power Operation and Torque Ripple Reduction", IEEE Transactions on Magnetics, Vol. 45, No. 10, pp. 4660-4663, Oct. 2009.
11. Ki-Chan Kim, "A Novel Calculation Method on the Current Information of Vector Inverter for Interior Permanent Magnet Synchronous Motor for Electric Vehicle"IEEE Transactions on Magnetics, Vol. 50, No. 2, Art. No. 7020504, Feb. 2014.
12. G. Liu, L. Liu, Q. Chen, and W. Zhao, "Torque Calculation of Five-Phase Interior Permanent Magnet Machine Using Improved Analytical Method", IEEE Transactions Energy Conversion, Vol. 34, No. 2, pp. 1023-1032, Jun. 2019.
13. L. Zhu, S. Z. Jiang, Z. Q. Zhu, and C. C. Chan, "Analytical Modeling of Multi-segment and Multilayer Interior Permanet Magnet Machines", in Proc. 17th Int. Conf. Elect. Mach. Syst., Oct. 2014, pp 28-33.
14. Duanek Hanselman, "Brushless Motors : Magnetic design, Performance, and control", E-Man Press LLC, pp. 656, 2012.
15. J.R. Hendershot, Jr and T.J.E. Miller, "Design of Brushless Permanent-Magnet Machines", Motor Design Books LLC, pp. 798, 2015.
16. Conggan Ma, Jingjing Zhang, Jianfeng Wang, Na Yang, Oinghe Liu, Shuguang Zuo, Xudong Wu, Puwei Wang, Jiaming Li, and Jianguang Fang, "Analytical Model of Open-Circuit Air-Gap Field distribution in Interior Permanent Magnet Machines Based on Magnetic Equivalent Circuit Method and Boundary Condistions of Macroscopic Equations", IEEE Transactions on magnetics, Vol. 57, No. 3, Mar. 2021.